THE JOURNAL OF PHYSICAL CHEMISTRY B

pubs.acs.org/JPCB Article

Mixed Quantum Classical Simulations of Charge-Transfer Dynamics in a Model Light-Harvesting Complex. II. Transient Vibrational Analysis

Published as part of The Journal of Physical Chemistry virtual special issue "Peter J. Rossky Festschrift".

Kush Patel and Eric R. Bittner*

Cite This: *J. Phys. Chem. B* 2020, 124, 2158–2167

Read Online

ACCESS | Metrics & More | Article Recommendations

ABSTRACT: We perform dynamics simulations of donor–bridge–acceptor triads following photoexcitation and correlate nuclear motions with the charge-transfer event using the short-time Fourier transform technique. Broadly, the porphyrin bridges undergo higher energy vibrations, whereas the fullerene acceptors undergo low energy modes. Aryl side groups exhibit torsional motions relative to the porphyrin. Aryl linkers between the bridge and acceptor are restricted from such motions and therefore express ring distortion modes. Finally, we find an amide linker mode that is directionally sensitive to electron motion. This work supports the notion of vibrationally coupled ultrafast charge transfer found in both experimental and theoretical studies and lays a foundational method for identifying key vibrational modes for parametrizing future theoretical models.

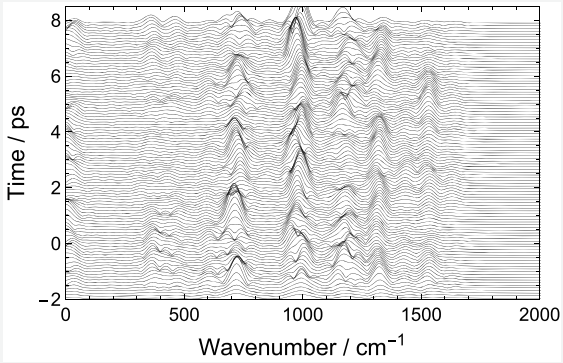

INTRODUCTION

A growing number of studies recognize vibrational dynamics as a key controlling factor in the electron transfer process of molecular systems.[1−7] Identifying the exact nature of the electron–nuclear motion is no trivial feat. In condensed phases, vibrational specificity is rapidly lost due to relaxation into intermolecular modes.[8,9] In previous works, our heuristic approach indicated that pervasive low energy modes (often of energies $\approx kT$) modulate electronic states at donor/acceptor heterojunction interfaces.[10,11] Response to photoexcitation and thermal fluctuation changes low-lying electronic excited states between localized excitonic to charge separated in character.

In energetically and spatially isolated environments, vibrational excitations persist for much longer time periods.[12−16] Furthermore, localized dynamics in linker molecules have a remarkable influence on molecular photophysics. Selective vibronic excitation of acetylene linkers in Pt(II) *trans*-acetylide assemblies can inhibit CT altogether.[16−18] Conversely, amide functional groups seem to be particularly sensitive to current. Previous work indicates rectification behavior as well as vibrational sensitivity, hinting toward a possible probe for CT dynamics.[19−21]

A deeper understanding of the interplay between electronic and nuclear degrees of freedom is therefore crucial for a robust description of soft photovoltaic materials and will provide insight toward fine-tuning materials toward high-efficiency photoconversion. In the accompanying paper, we detailed a method to approximate charge-transfer rates in donor–bridge–acceptor triads wherein each constituent moiety is a highly conjugated organic molecule (Figure 1). Our approach combines quantum mechanical treatment of π-electrons with molecular mechanics treatment of nuclei and σ-electrons (force fields), enabling a significant speed up of dynamics simulations over fully quantum mechanical methods. Our results show comparable CT rates to those derived both experimentally and theoretically. In the present work, we make use of signal processing techniques to analyze transient nuclear motions to qualitatively characterize dynamics occurring in the ensembles and identify the relevant vibrational modes active and inactive in relation to the electron transfer process.

THEORETICAL METHODS

It is important to quantify which nuclear motions are most strongly correlated to the electronic charge-transfer event. For this, we use the velocity autocorrelation function

Received: January 9, 2020
Revised: February 25, 2020
Published: March 2, 2020

https://dx.doi.org/10.1021/acs.jpcb.0c00203
J. Phys. Chem. B 2020, 124, 2158–2167

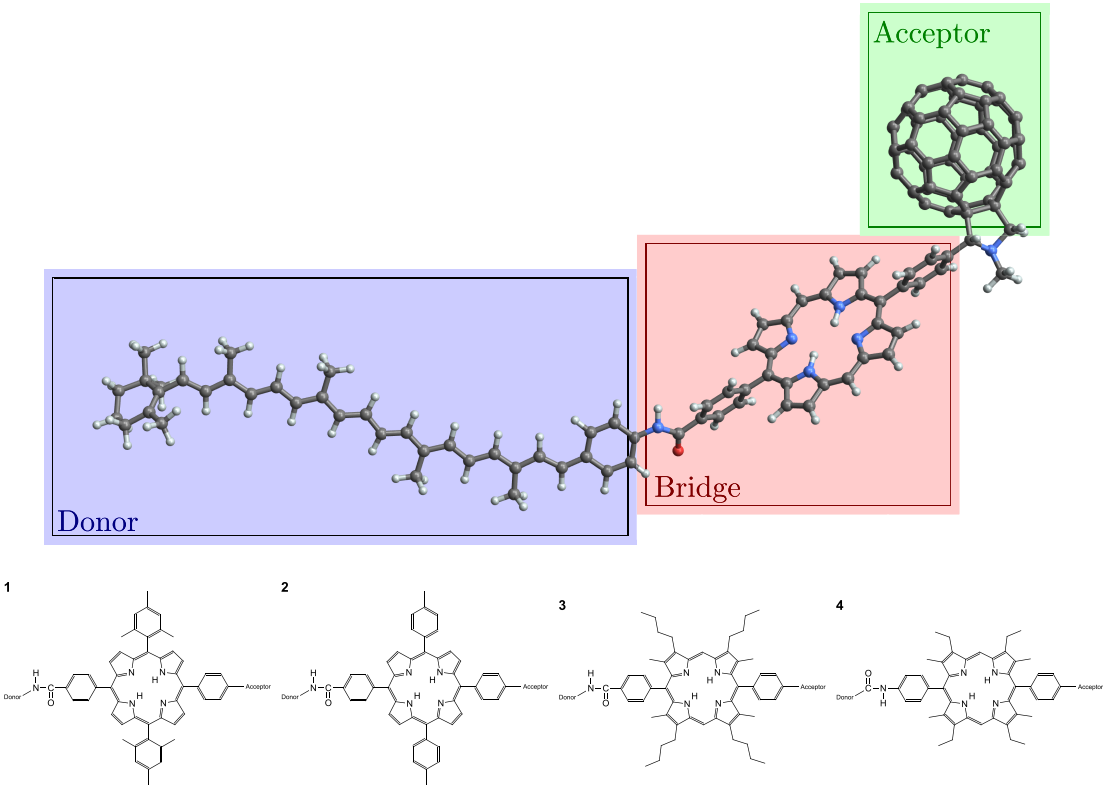

Figure 1. (Top) Basic construction of the donor−bridge−acceptor triad composed of a carotenoid donor (blue), porphyrin bridge (red), and fullerene derivative acceptor (green). Alternative structures include addition of side groups to the porphyrin in β or *meso* positions, increasing the distance between subunits via methylene units or a different fullerene derivative. (Bottom) The bridging moieties differentiate the molecules.

$$C_{vv}(\tau) = \sum_{t=0}^{T-\tau} \sum_{i} \vec{v}_i(t) \cdot \vec{v}_i(t+\tau) \tag{1}$$

where τ is the lag time; T is the total time; index i spans the list of particles considered; and $\vec{v}_i(t)$ is the velocity of particle i at time t. Fourier transform of the correlation function gives a power spectrum detailing the relative prevalence of vibrational modes. However, this only provides a time-averaged description and is only well-suited for a stationary signal; it does not decode information about transient signals.

Certain nuclear modes will activate and deactivate during the charge-transfer process. A time−frequency spectrogram of a nonstationary time series will resolve evolution of the vibrational power spectrum.[22] For this, we apply the short-time Fourier transform (STFT) method on the velocity autocorrelation function to visualize the evolution of the nuclear dynamics in time

$$S(\tau, \omega) = \int_{-\infty}^{\infty} f(t) g(t-\tau) \mathrm{e}^{-\mathrm{i}2\pi\omega t} dt \tag{2}$$

$$g(t-\tau) = \begin{cases} \frac{1}{2} - \frac{1}{2}\cos\left(\frac{\pi(\tau - t + \mathcal{T})}{\mathcal{T}}\right) & |\tau - t| \le \mathcal{T} \\ 0 & |\tau - t| > \mathcal{T} \end{cases} \tag{3}$$

where $\mathcal{T}$ is the window radius of the Hanning window function $g(t)$, defined in eq 3. Nakai and co-workers have used this technique for the analysis of *ab initio* dynamics simulations of small-molecule collision reactions.[23−28] STFT resolution is restricted to the Heisenberg−Gabor limit such that wider window functions resolve frequencies better but sacrifice time resolution, whereas thinner windows give better time resolution but sacrifice frequency resolution.[29,30] For a given window radius, uncertainty in frequency can be computed as $\Delta\omega \approx (2cT)^{-1}$. STFT was performed with a Hanning window of width $\mathcal{T} = 600$ fs ($\Delta\omega \approx 28$ cm^{-1}). At this resolution, we may not be able resolve finer details of the vibrational spectrograph, but it is sufficiently suitable for our needs. Edge effects occur as a result of this analysis on finite time series. At the temporal extrema, less information is available, resulting in an overall smoothing and diminishing of the spectral intensity. To mitigate this, we include dynamics from 2 ps prior to the photoexcitation.

The discrete STFT process returns a two-dimensional array in time and frequency. By plotting the spectrogram, we can filter out modes that are activated or deactivated over the charge-transfer event. The process is as follows:

1. Shift the intensities down for a mode's (ω_k) spectral time series such that its average lies at 0

$$\tilde{S}(\tau, \omega_k) = S(\tau, \omega_k) - s_k \tag{4}$$

for some s_k

$$\int_{t_1}^{t_2} \tilde{S}(\tau, \omega_k) \mathrm{d}\tau = 0 \tag{5}$$

where t_1 and t_2 are the temporal limits of the vibrational time considered.

https://dx.doi.org/10.1021/acs.jpcb.0c00203
J. Phys. Chem. B 2020, 124, 2158−2167

2. Define a rectangle function that is unity in the charge-transfer time span and zero otherwise and again shift it down so that its average value is 0.

$$\int_{t_1}^{t_2} \mathrm{Rect}(\tau)\mathrm{d}\tau = 0 \tag{6}$$

3. The inner product of the shifted spectral time series, $\tilde{S}$, and the shifted rectangle function

$$C(\omega_k) = \int_{t_1}^{t_2} \tilde{S}(\tau, \omega_k)\mathrm{Rect}(\tau)\mathrm{d}\tau \tag{7}$$

gives a correlation strength between the mode and the charge-transfer process. A large positive value indicates direct correlation: the mode is specifically active during the charge transfer. A large negative value indicates the mode is inactive during charge transfer and it is active otherwise. Small correlation values indicate either poor correlation or low spectral amplitude, either of which implies the mode is of no interest. Thus, this analysis gives a compact value that relates the activity of a mode to the charge-transfer process.

Time-series plots and rate histograms from the accompanying paper clearly indicate that the charge-transfer event varies across all trajectories, and simply averaging over every trajectory will not reveal which specific modes are activated or deactivated while charge transfer occurs. As a filter, we choose a subensemble of trajectories for each molecule which exhibit similar charge-transfer character. For this, we define the following metric for the difference between two trajectories. Let $q_i(t)$ and $q_j(t)$ be two logistic regressions (defined in the accompanying paper) for trajectories indexed i and j. The integrated difference then is given by

$$\varepsilon_{ij} = \int_{t_1}^{t_2} (q_i(t) - q_j(t))^2 \mathrm{d}t \tag{8}$$

for t_1 and t_2 defining the time window considered. Identical functions clearly result in a vanishing integral, and deviations result in increasingly larger ϵ. We choose the set of 10 trajectories, for each molecule, which mutually give the smallest collective difference integral. Since the Fourier transform and STFT are linear operations, the average spectrogram can be achieved by averaging the autocorrelations of the trajectories chosen and then performing the transform.

Each molecule simulated contains between 238 and 272 atoms which leads to over 750 normal modes. The entire triad is a highly conjugated system whose moieties themselves are conjugated subsystems. Naturally, these subsystems have overlapping vibrational spectra wherein spectral intensity from some modes of one moiety could be washed out by that of another moiety. While this indicates such modes are weaker relative to the total system, they still may be relevant to the CT process, considering the entire molecule as a whole may obscure crucial results. By considering where the differences in construction between molecules lie or crucial points in the molecule (linkers), we can isolate the necessary atomic subsets, perform an autocorrelation of their velocities, and perform the STFT to reveal the underlying dynamics. We screen the resulting spectrograms for modes relative to the charge-transfer process. The temporal limits for screening, t_1 and t_2, are defined by the 5% and 95% CT completion times to sufficiently encapsulate the region of interest.

RESULTS

Aromatic Bridge Side-Chain Dynamics. We first consider molecules **M1** and **M2**. Here, the major difference is the number of methyl groups on the *meso* aryl side groups attached to the porphyrin. In Figure 2 we present the STFT

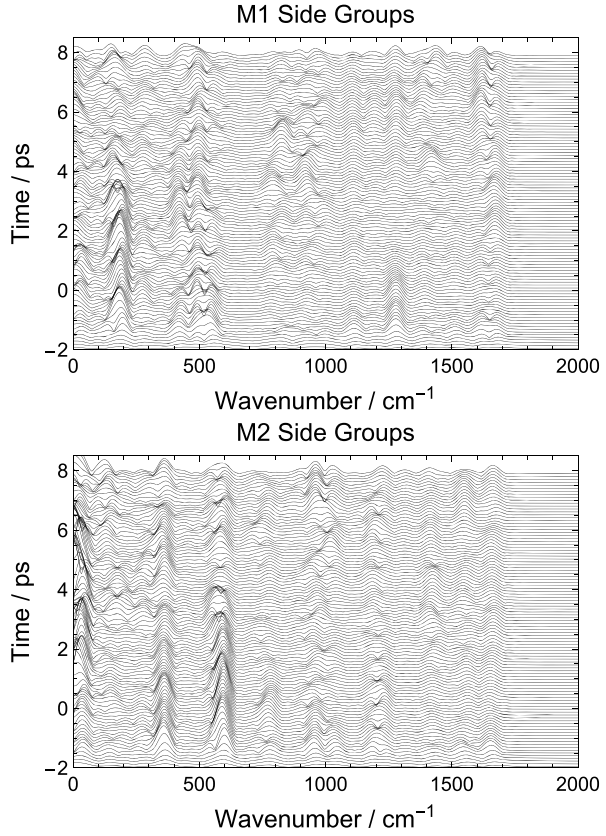

Figure 2. STFT spectrograms for **M1** (top) and **M2** (bottom) aryl side groups on the bridge.

spectrograms for these two systems. It is immediately noticeable that modes of energies higher than 700 cm^{-1} are of low intensity or absent altogether. Typical vibrational spectra for mesityl and toluene reveal modes at 700−800 cm^{-1} (out-of-plane ring distortions) and 1500 cm^{-1} (C═C stretches). The low energy vibrations that are present are torsional modes; the side aryl rings are rotating across the bond which links them to the porphyrin bridge. We confirm this by computing the time series of the dihedral angle of these groups to the porphyrin. Simple Fourier transform of these time series reveals spectral intensities centered at the same frequency in the STFT spectrograms (Figure 3, top).

Regarding **M1**, two modes at 190 and 425 cm^{-1} are found in all three visualizations, confirming both the torsional dynamics and relevance to the CT process. The dihedral angle here modulates the amount of p_z orbital overlap and therefore has a nonzero effect on the local electronic structure of the bridge. A previous calculation gives the first excitation energy dependence on the dihedral angle of an idealized configuration of an isolated porphyrin, plotted in Figure 4. The computation reveals only a 0.1 eV difference between 0° (full p_z overlap) and 90° (no p_z overlap). However, given the amount of steric hindrance experienced, the accessible angle space is constrained around 72° (±4°), and the excitation energy only

https://dx.doi.org/10.1021/acs.jpcb.0c00203
J. Phys. Chem. B 2020, 124, 2158−2167

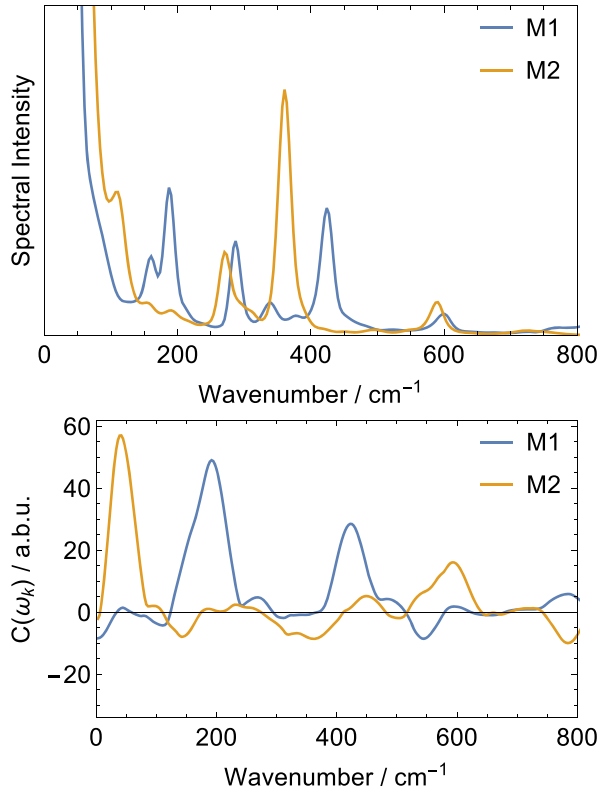

Figure 3. (Top) Fourier transform of the dihedral angle time series between the bridge and its aryl side groups for **M1** and **M2**. (Bottom) Screened STFT modes for the same subunits in **M1** and **M2**. Both figures here are featureless for wavenumbers above 800 cm^{-1}.

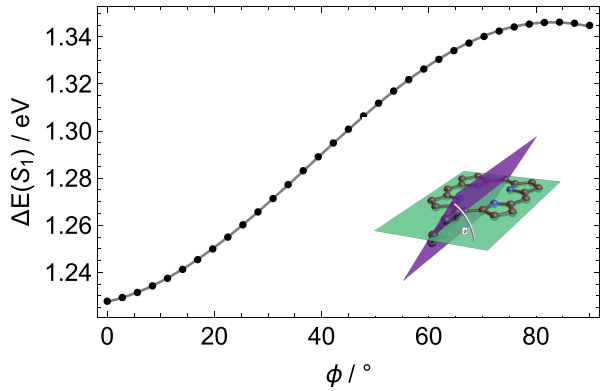

Figure 4. First excitation energy of isolated diaryl *meso*-substituted porphyrin dependence on dihedral angle, ϕ, as indicated on the inset structure. Points correspond to calculated energies. Gray curve corresponds to a curve fit. Fit: $\Delta E(\phi) = E_{max} - \delta E^* \cos^2(\phi + \gamma)$, E_{max} = 1.35 eV, δE = 0.12 eV, and γ = 0.12 (radians).

changes by single-digit meV. Thus, for practical purposes, the dihedral angle of these conjugated side groups has little effect on the bridge electronic structure and therefore CT. Despite this, we can conclude there is still some interplay between the CT process and this particular mode: in the context of vibronic transitions, excitation of this mode certainly accompanies the π–π^* electronic excitation.

With less steric hindrance, **M2** has a much stronger response from the 360 cm^{-1} torsional mode; however, this mode is generally active throughout the simulation time and therefore does pass screening. Conversely, the strong 600 cm^{-1} mode correlates to CT but is not prominent in the dihedral spectrum; therefore, this is likely to be some low energy ring distortion. Charge transfer in **M2**, then, seems unaffected by torsional motions of the aryl side groups. We make the same arguments as with **M1**; these modes are activated during the initial excitation but do not play an essential role in electronic relaxation of the system into a charge-transfer state.

Bridge Moiety Linker Dynamics. We next consider **M3** and **M4**. The bridge side groups here are not π active and, similar to the previous molecules, do not have a significant impact on the electronic structure of the bridge directly. From an experimental standpoint, aliphatic substituents like these are included to control the solubility of the molecule. However, as pointed out by Bahr, the longer chains in the β positions sterically interfere with and force the linker aryl groups into orthogonal orientations.[31] The dihedral angle of these linkers to the porphyrin should have a much larger impact on CT over the side aryl groups. The increased orbital overlap between porphyrin and these linkers extends the molecular π orbital toward the fullerene acceptor and therefore increases the electronic interaction between the two subsystems. Figure 5

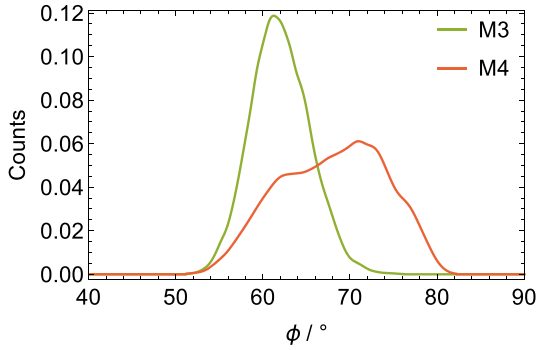

Figure 5. Distribution of dihedral angles sampled by the aryl linker between the bridge and acceptor moieties during dynamics for **M3** and **M4**.

plots a smooth histogram distribution of the dihedral angles sampled by these linkers. Curiously, our dynamics results show a contrary trend. The linker in **M3** is constrained to a smaller angle space, but this space is not orthogonal, averaging just over 60°. The linker in **M4** accesses a wider angle space and, although sterically allowed to have a more planar angle, tends to be closer to orthogonal.

STFT spectrograms for these subunits are found in Figure 6. The low frequency modes (390 and 600 cm^{-1}) are muted in **M3**. These frequencies appear in the dihedral angle times series analysis (Figure 7, top), and thus we define both as torsional modes. When screened, the former mode is of no interest, but the latter mode shows as strongly anticorrelated. Low spectral intensity in STFT is consistent with the narrow distribution of angles sampled. We argue here that as electron density travels through the linker the angle with the bridge plane is locked in place. A mode at 950 cm^{-1} has a strong response at an early time and then slowly decays. This mode is likely activated by the photoexcitation but diminishes once CT begins. Furthermore, it does not appear in the dihedral analysis and therefore is likely to be a ring distortion mode. Of lower overall intensity, the 1010 cm^{-1} mode shows some response following excitation and then increased activity during CT and finally decaying after that. Weaker still, the 1570 cm^{-1} mode

https://dx.doi.org/10.1021/acs.jpcb.0c00203
J. Phys. Chem. B 2020, 124, 2158–2167

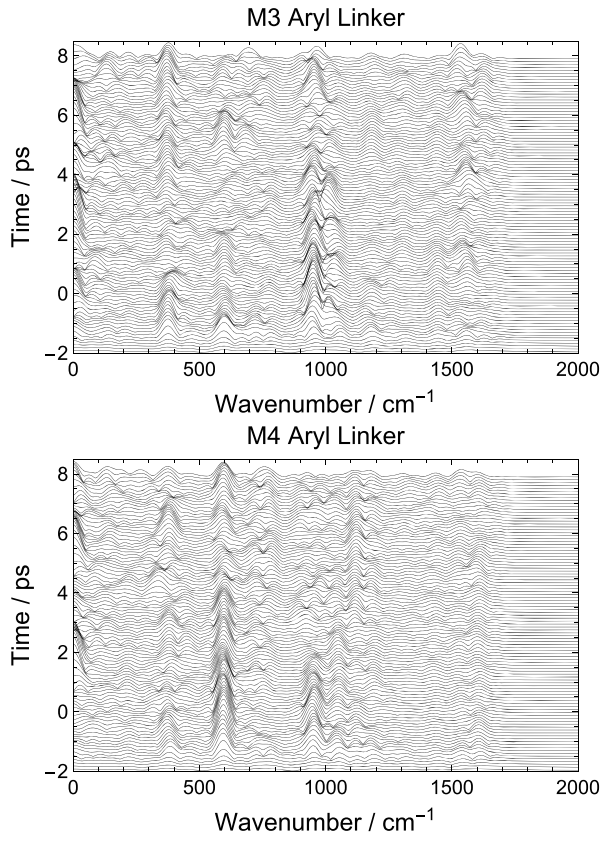

Figure 6. STFT spectrograms for an aryl linker between the bridge and acceptor in **M3** (top) and **M4** (bottom).

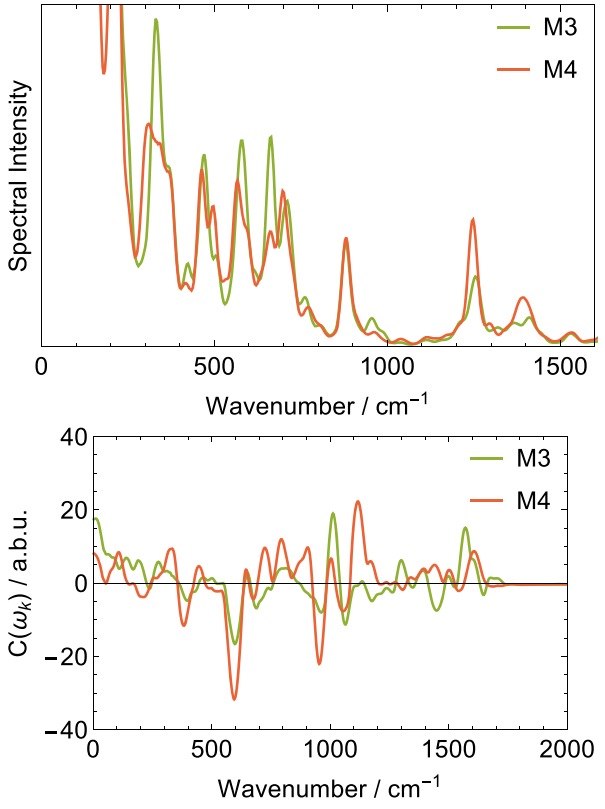

Figure 7. (Top) Fourier transform of the dihedral angle time series between the bridge and the aryl ring which links bridge and acceptor moieties for **M3** and **M4**. Figure is featureless for wavenumbers above 1500 cm^{-1}. (Bottom) Screened STFT modes for the same subunits in **M3** and **M4**.

shows as highly correlated. We determine these last two modes as ring vibrations as they do not appear in the dihedral angle analysis.

Spectra for the linker in **M4** reveal the presence of similar modes to that of **M3**. The 390 cm^{-1} mode appears anticorrelated but has a far too weak intensity to have significance. Contrary to **M3**, the 600 cm^{-1} frequency here is not only highly active but also, as a result, strengthens the anticorrelation. Intense activity of this mode before CT corroborates with the wide range of angles sampled; however, torsion is restricted once current flows through the linker. The temporal shape of the 950 cm^{-1} mode largely mimics that of the 600 cm^{-1} mode in **M3** but with larger intensity: this mode is active at photoexcitation but absent thereafter. Two final vibrational modes at 1120 and 1600 cm^{-1} are relatively weak in the STFT spectrogram; however, they are still correlated to CT.

Amide linker STFT spectrograms are plotted in Figures 8 and 9. Prevalent for all four molecules are intense features at 700, 1000, 1200, and 1300−1400 cm^{-1}. Upon screening these modes in time, only the 700 and 1200 cm^{-1} appear to play significant roles. The first is the low energy 700 cm^{-1} mode. Vibrational computation on formamide suggests this mode is a twisting motion along the C−N bond. In **M1** and **M2**, this mode is sporadically activated and deactivated (Figure 10). However, there is a stark difference with **M3** and **M4**, recalling that direction of this linker is reversed between the two. **M3** has the favorable orientation, according to the rectification bias,[20] to allow electron density to pass from the donor to the bridge. In our studies, this mode correlates extremely well with CT to the acceptor. Naturally, the net positive charge in the bridge will begin to attract electron density from the donor. In **M4**, the amide is in the unfavorable orientation, and we show here that the 700 cm^{-1} mode is turned off during the bridge to acceptor CT. We reasonably conclude that this particular mode is highly sensitive to the direction of current passing through the amide. The mode in the region of 1200 cm^{-1} (Amide I: C−N stretch, C−N−H bend) is universally off during CT in all four molecules, indicating this mode is not conducive to CT. In contrast to the findings published in ref 21, we see no activity in amide modes above 1500 cm^{-1} and therefore cannot comment on the sensitivity of the 1700 cm^{-1} mode to the electronic structure.

Bridge Dynamics. We turn our attention now to the bridging moiety. STFT spectrograms are found in Figures 11 and 12. Mode screening for the four bridges is found in Figure 13. What is immediately obvious between the four spectrograms is the general absence of features under 500 cm^{-1} and above 1500 cm^{-1}. Previous ground-state experimental and computational vibrational studies of water-solvated (free base and select derivatives of) porphyrin[32] agree that these wavenumber regions are generally featureless. **M1** and **M2** see some low energy modes at 500 and 600 cm^{-1}, respectively, that strongly correlate with CT. These macromolecular modes are not present in **M3** or in **M4**, and we speculate these modes resemble ring twisting with nodes at the *meso* position atoms. Such modes would alter the aromaticity of the ring (breaking planarity and therefore having a marked impact on electronic structure) but would be far more restricted by the heavier alkyl β substitutions with **M3** and **M4**. The 720 cm^{-1} mode, likely

https://dx.doi.org/10.1021/acs.jpcb.0c00203
J. Phys. Chem. B 2020, 124, 2158−2167

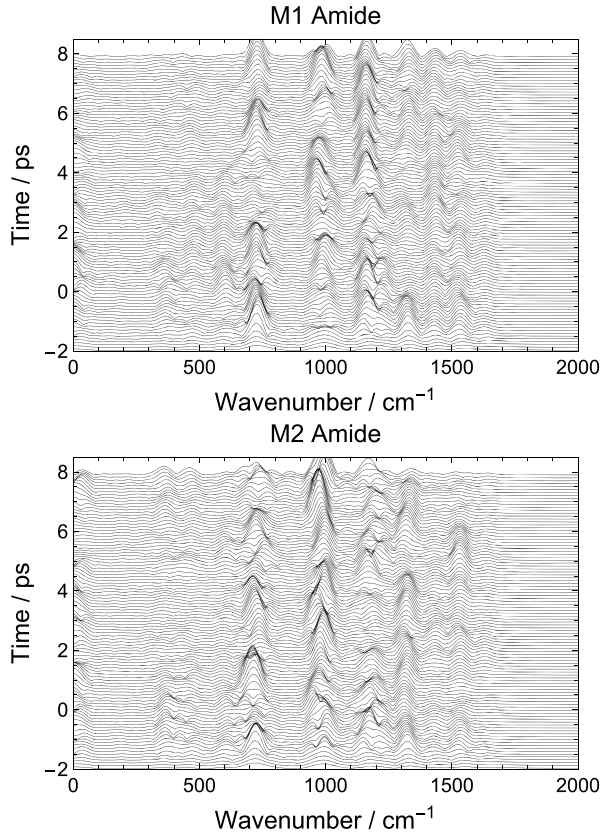

Figure 8. STFT spectrograms for the amide linker in **M1** (top) and **M2** (bottom).

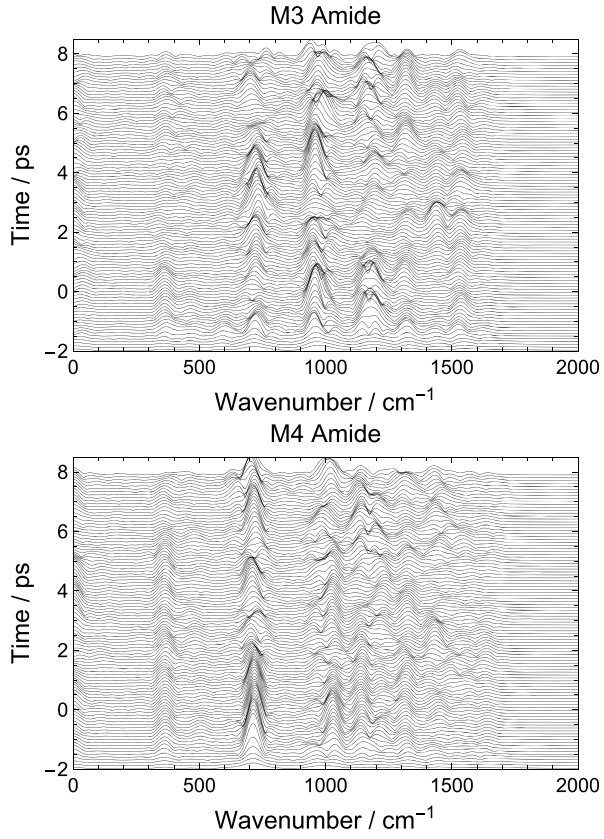

Figure 9. STFT spectrograms for the amide linker in **M3** (top) and **M4** (bottom).

some alternative ring deformation, is active in all four molecules and is anticorrelated with the CT, excluding **M3** where it shows as uncorrelated. The intensity of this mode is oscillatory throughout the dynamics, activated universally at the time of excitation, and then progressed with seemingly inconsistent behavior.

In the 950−1050 cm^{-1} vibrational region, **M1** and **M4** show CT correlation, while **M2** and **M3** show anticorrelation with spectral intensities differing between all four molecules. **M1** solely sees a strongly anticorrelated mode at 1110 cm^{-1}. This mode in both **M1** and **M2** is activated at excitation then decays in time; however, the mode reemerges after CT in **M1**. The same frequency in **M3** and **M4** is almost entirely nonexistent, lending to the idea this mode is ring torsion with nodes at *meso* atoms. Most nuclear displacement would occur at the pyrrole rings which would be inhibited by heavy β substituents. Finally, a mode in the mid 1400 cm^{-1} range shows as correlated in **M2**, anticorrelated in **M3**, and decorrelated in **M1** and **M4**. These modes are of low intensity overall, and temporal behavior is universally noisy, perhaps only coincidentally aligned (misaligned) with CT in **M2** (**M3**).

Acceptor Dynamics. We conclude our analysis by examining the nuclear modes localized on the fullerene acceptor. The STFT spectrograms for these are shown in Figures 14 and 15, and the mode screening for the acceptors can be found in Figure 16. Contrary to the bridge counterparts, the acceptors have much more activity in the low-frequency range and relatively subdued activity at higher frequencies. In general, the spectrograms reveal that most of the dynamical activity is in breathing or other macromolecular modes as opposed to local carbon−carbon stretches. Computational

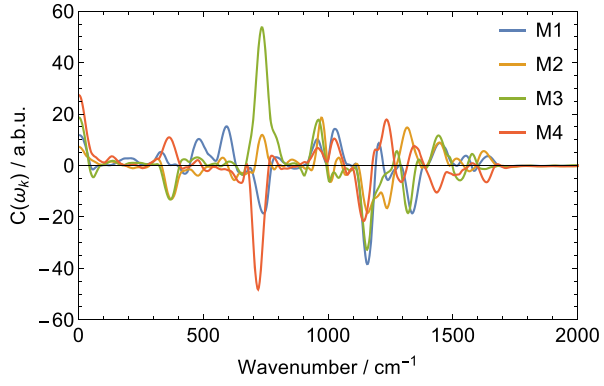

Figure 10. Screened vibrational modes for the amide linker in **M1**−**4**.

optimization (DFT/B3LYP level) of C_{60} fullerenes concludes that the ionic forms have larger overall radii and distortion of the spherical geometry versus the neutral molecule.[33] We expect to see breathing modes accompany electronic charging of this moiety, and all four molecules show some level of correlation to CT with a mode between 200 and 250 cm^{-1} with **M4** having a strong correlation. A multitude of other modes show a strong correlation in either direction (e.g., 500, 700, 1000−1200 cm^{-1}) but are not consistent through each molecule despite this moiety being identical throughout. **M2** does have a strongly anticorrelated mode just under 1500 cm^{-1}. This mode is active at a consistent intensity through the simulation time in the other molecules and hence gives a low correlation.

https://dx.doi.org/10.1021/acs.jpcb.0c00203
J. Phys. Chem. B 2020, 124, 2158−2167

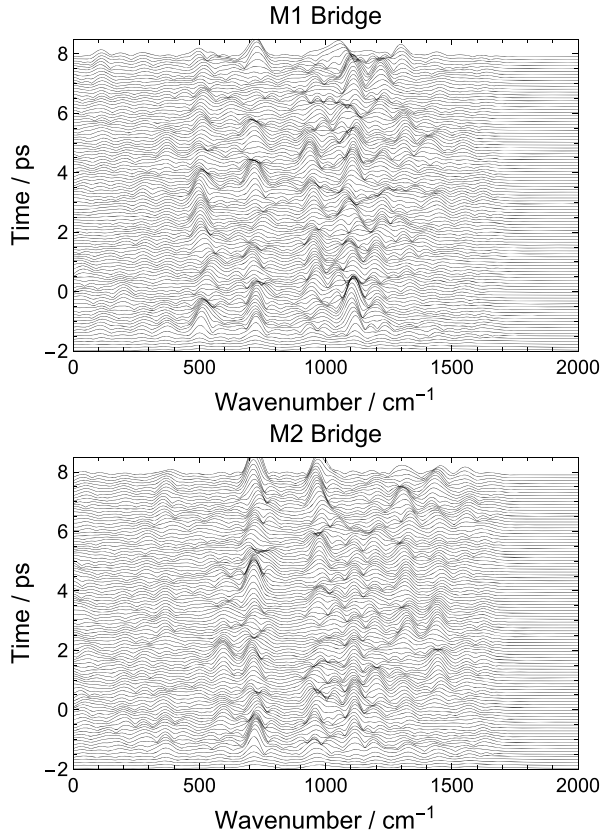

Figure 11. STFT spectrograms for the porphryin bridge in **M1** (top) and **M2** (bottom).

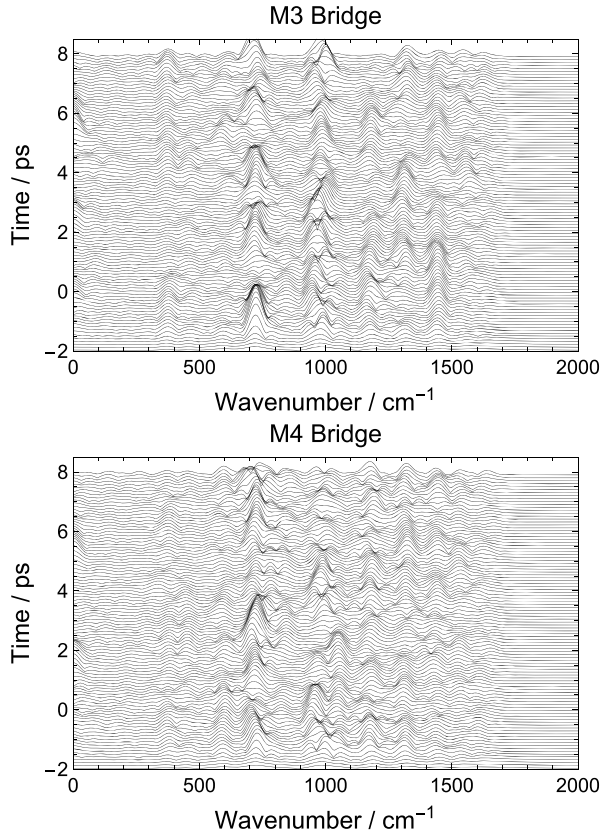

Figure 12. STFT Spectrograms for the porphryin bridge in **M3** (top) and **M4** (bottom).

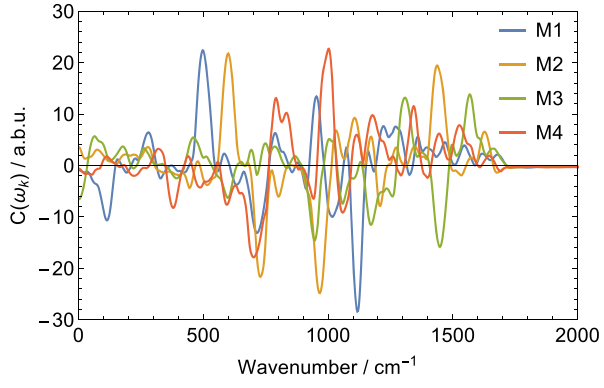

Figure 13. Screened vibrational modes for the porphyrin moiety in **M1−4**.

Summary. Vibrational energy within the porphyrin is primarily distributed among higher frequency modes, which is likely associated with the large electronic excitation energy pumped into a localized region. The fullerene, conversely, has most of its vibrational energy distributed among low energy modes. Outside of the modes mentioned above, no other modes seem to behave consistently across these triads, at least temporally. The inconsistency in vibrational behavior could be due to a few reasons. Our subset for STFT analysis chooses only 10 trajectories, which may be an insufficient number for analyzing larger structures. Analysis of linker and bridge side groups involved at most 12 atoms, limiting the total number of normal coordinates, whereas the same analysis of full moieties requires the consideration of 30 atoms and upward. A large number of degrees of freedom give rise to more vibrational modes that are both energetically similar (possibly degenerate) and energetically accessible. Alternatively, the dynamics of the triads seems to depend on the initial conditions. Variations in the geometries necessarily result in varying excitation energies and excited electronic structures which in turn give diverse charge-transfer characteristics. Therefore, averaging more trajectories would either reduce the vibrational noise resulting from the increase in accessible modes or, if noise is not reduced, give further credence to the sensitivity to initial conditions.

An additional effect of the dynamical evolution of force constants with the electronic structure is the blue- or red-shifting of the vibrational modes, and this can be seen most prominently in the amide STFT spectrograms. Within the harmonic oscillator approximation, the frequency of a mode is proportional to the square root of the force constant which is modulated by the π bond order (off-diagonal elements of the site basis density matrix). The most extreme case of this shift is around 50 cm^{-1} seen in the 1000 cm^{-1} mode in Figure 2 (bottom), whereas this effect is less pronounced in other spectrograms. While this shift should be an indicator of fluctuating electronic state, our choice of time−frequency analysis and window function width in this work gives a frequency uncertainty of about 28 cm^{-1}, and consequently, we reserve a detailed discussion of the effect in the present results. The trade-off between uncertainty in temporal or frequency resolution is unavoidable. However, the wavelet transform technique of time−frequency analysis does provide better resolution than STFT, and future analyses will benefit from this approach.[26,29,34]

https://dx.doi.org/10.1021/acs.jpcb.0c00203
J. Phys. Chem. B 2020, 124, 2158−2167

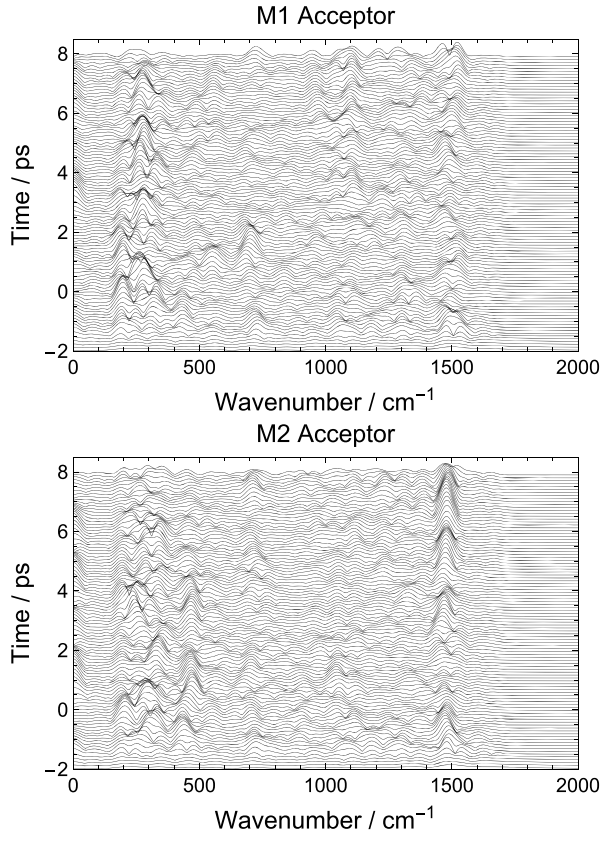

Figure 14. STFT spectrograms for the fullerene acceptor in **M1** (top) and **M2** (bottom).

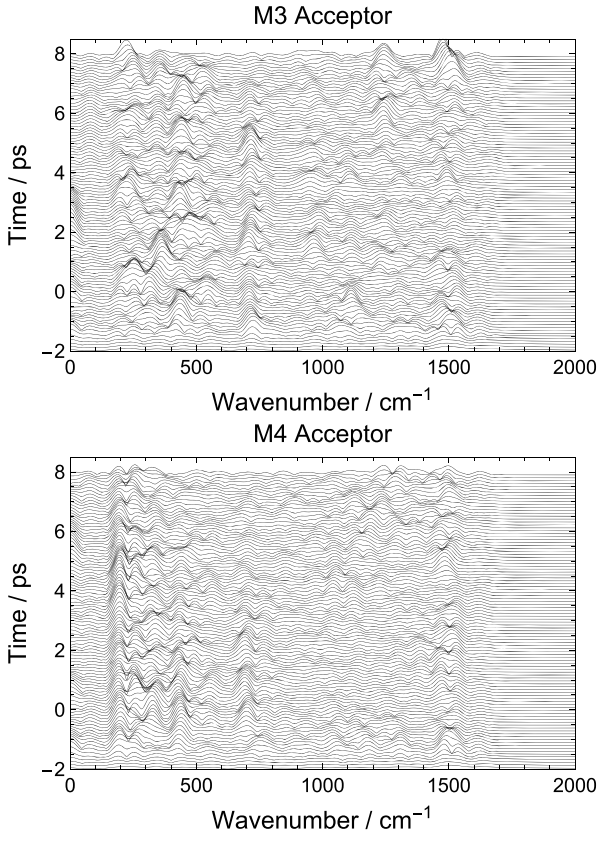

Figure 15. STFT spectrograms for the fullerene acceptor in **M3** (top) and **M4** (bottom).

CONCLUSIONS

We have provided here time-resolved vibrational power spectra which characterize the nuclear vibrations occurring in our simulations. Our mode filtering technique provides a qualitative correlation of vibrational modes to the initial charge-transfer process. By considering a subset of atoms from each triad, we can pinpoint which nuclear motions have the most active coupling to the electronic states. We find that conjugated aryl side groups on the porphyrin undergo dihedral rotations (lower energy) over ring breathing and ring distortions (higher energy). Despite a strong response to CT, such torsional motions have very little effect on the electronic structure of the porphyrin at large. Conversely, aryl rings which link the bridge and acceptor units are shown to have little torsional behavior, and instead, nuclear motions take the form of ring distortions. Although this work focuses on charge migration from the bridge to acceptor, we still analyze the vibrations of the amide linking bridge and donor units. Here we find with **M3** and **M4** a torsional mode that is sensitive to the direction of electron flow. Finally, our analysis of bridge and acceptor moieties shows very little commonalities in nuclear dynamics between triads specific to the CT, despite the level of similarity in chemical structure. Nuclear energy is broadly distributed among high energy ring distortion modes in the bridge and low energy breathing modes in the acceptor.

We do not at this time distinguish between modes *induced by* versus *facilitating* CT but do confirm correlation. In either case, we suspect such modes to have strong electron−vibrational coupling (large Huang−Rhys parameters (HRPs)[35]) and should certainly be included in theoretical models. Previously, our models considered few or common normal modes,[36−38] and this work lays foundational steps toward parametrizing such models with targeted specificity, leading to a more robust description. Computing the Huang−Rhys parameters poses a difficult challenge. The general prescription for computing HRPs requires minimizing the geometry of considered electronic states in addition to computing vibrational energies and corresponding normal coordinates.

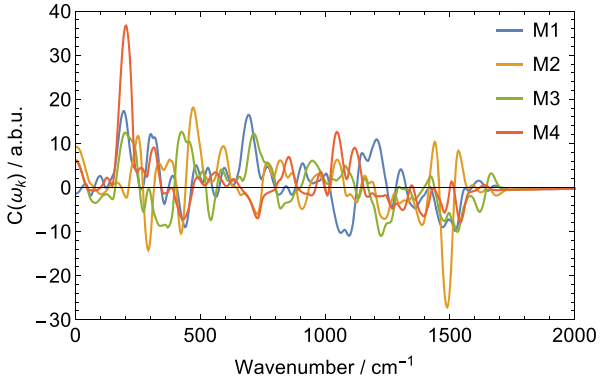

Figure 16. Screened vibrational modes for the acceptor moiety in **M1−4**.

https://dx.doi.org/10.1021/acs.jpcb.0c00203
J. Phys. Chem. B 2020, 124, 2158−2167

AUTHOR INFORMATION

Corresponding Author

Eric R. Bittner − *Department of Chemistry, University of Houston, Houston, Texas 77204, United States; Department of Physics, Durham University, Durham DH1 3LE, United Kingdom;* orcid.org/0000-0002-0775-9664; Email: ebittner@central.uh.edu

Author

Kush Patel − *Department of Chemistry, University of Houston, Houston, Texas 77204, United States;* orcid.org/0000-0003-0485-9982

Complete contact information is available at: https://pubs.acs.org/10.1021/acs.jpcb.0c00203

Notes

The authors declare no competing financial interest.

Our implementation of the TDHF/molecular dynamics is available as the πTDHF code on GitHub.

ACKNOWLEDGMENTS

The work at the University of Houston was funded in part by the National Science Foundation (CHE-1664971, MRI-1531814) and the Robert A. Welch Foundation (E-1337). E.R.B. acknowledges the Leverhulme Trust for support at Durham University.

REFERENCES

(1) Wiederrecht, G. P.; Niemczyk, M. P.; Svec, W. A.; Wasielewski, M. R. Ultrafast Photoinduced Electron Transfer in a Chlorophyll-Based Triad: Vibrationally Hot Ion Pair Intermediates and Dynamic Solvent Effects. *J. Am. Chem. Soc.* **1996**, *118*, 81−88.

(2) Blanchet, V.; Zgierski, M. Z.; Seideman, T.; Stolow, A. Discerning vibronic molecular dynamics using time-resolved photoelectron spectroscopy. *Nature* **1999**, *401*, 52−54.

(3) Davis, W. B.; Ratner, M. A.; Wasielewski, M. R. Conformational Gating of Long Distance Electron Transfer through Wire-like Bridges in Donor−Bridge−Acceptor Molecules. *J. Am. Chem. Soc.* **2001**, *123*, 7877−7886.

(4) Kushmerick, J. G.; Lazorcik, J.; Patterson, C. H.; Shashidhar, R.; Seferos, D. S.; Bazan, G. C. Vibronic Contributions to Charge Transport Across Molecular Junctions. *Nano Lett.* **2004**, *4*, 639−642.

(5) Shizu, K.; Sato, T.; Tanaka, K.; Kaji, H. Electron−Vibration Interactions in Triphenylamine Cation: Why are Triphenylamine-Based Molecules Good Hole-Transport Materials? *Chem. Phys. Lett.* **2010**, *486*, 130−136.

(6) Sukegawa, J.; Schubert, C.; Zhu, X.; Tsuji, H.; Guldi, D. M.; Nakamura, E. Electron Transfer through Rigid Organic Molecular Wires Enhanced by Electronic and Electron−Vibration Coupling. *Nat. Chem.* **2014**, *6*, 899−905.

(7) Hashimoto, S.; Yabushita, A.; Iwakura, I. Real-Time Observation of Interfragment Vibration and Charge Transfer within the $TCNQF_4$ Dimer. *Chem. Phys.* **2017**, *493*, 56−60.

(8) Shapiro, M.; Brumer, P. Coherent Control of Molecular Dynamics. *Rep. Prog. Phys.* **2003**, *66*, 859−942.

(9) Briney, K. A.; Herman, L.; Boucher, D. S.; Dunkelberger, A. D.; Crim, F. F. The Influence of Vibrational Excitation on the Photoisomerization of trans−Stilbene in Solution. *J. Phys. Chem. A* **2010**, *114*, 9788−9794.

(10) Bittner, E. R.; Kelley, A. The Role of Structural Fluctuations and Environmental Noise in the Electron/Hole Separation Kinetics at Organic Polymer Bulk-Heterojunction Interfaces. *Phys. Chem. Chem. Phys.* **2015**, *17*, 28853−28859.

(11) Kelley, A.; Patel, K.; Bittner, E. R. Quantum Simulations of Charge Separation at a Model Donor-Acceptor Interface: Role of Delocalization and Local Packing. *Adv. Condens. Matter Phys.* **2018**, *2018*, 1−10.

(12) Hamm, P.; Lim, M.; Hochstrasser, R. M. Vibrational Energy Relaxation of the Cyanide Ion in Water. *J. Chem. Phys.* **1997**, *107*, 10523−10531.

(13) Zhong, Q.; Baronavski, A. P.; Owrutsky, J. C. Vibrational Energy Relaxation of Aqueous Azide Ion Confined in Reverse Micelles. *J. Chem. Phys.* **2003**, *118*, 7074−7080.

(14) Kasyanenko, V. M.; Lin, Z.; Rubtsov, G. I.; Donahue, J. P.; Rubtsov, I. V. Energy Transport via Coordination Bonds. *J. Chem. Phys.* **2009**, *131*, 154508.

(15) Park, K. H.; Jeon, J.; Park, Y.; Lee, S.; Kwon, H. J.; Joo, C.; Park, S.; Han, H.; Cho, M. Infrared Probes Based on Nitrile-Derivatized Prolines: Thermal Insulation Effect and Enhanced Dynamic Range. *J. Phys. Chem. Lett.* **2013**, *4*, 2105−2110.

(16) Delor, M.; Sazanovich, I. V.; Towrie, M.; Spall, S. J.; Keane, T.; Blake, A. J.; Wilson, C.; Meijer, A. J. H. M.; Weinstein, J. A. Dynamics of Ground and Excited State Vibrational Relaxation and Energy Transfer in Transition Metal Carbonyls. *J. Phys. Chem. B* **2014**, *118*, 11781−11791.

(17) Delor, M.; Sazanovich, I. V.; Towrie, M.; Weinstein, J. A. Probing and Exploiting the Interplay between Nuclear and Electronic Motion in Charge Transfer Processes. *Acc. Chem. Res.* **2015**, *48*, 1131−1139.

(18) Delor, M.; Keane, T.; Scattergood, P. A.; Sazanovich, I. V.; Greetham, G. M.; Towrie, M.; Meijer, A. J.; Weinstein, J. A. On the Mechanism of Vibrational Control of Light-Induced Charge Transfer in Donor-Bridge-Acceptor Assemblies. *Nat. Chem.* **2015**, *7*, 689−695.

(19) Aviram, A.; Ratner, M. A. Molecular Rectifiers. *Chem. Phys. Lett.* **1974**, *29*, 277−283.

(20) Ding, W.; Negre, C. F. A.; Vogt, L.; Batista, V. S. Single Molecule Rectification Induced by the Asymmetry of a Single Frontier Orbital. *J. Chem. Theory Comput.* **2014**, *10*, 3393−3400.

(21) Sun, X.; Zhang, P.; Lai, Y.; Williams, K. L.; Cheung, M. S.; Dunietz, B. D.; Geva, E. Computational Study of Charge-Transfer Dynamics in the Carotenoid−Porphyrin−C_{60} Molecular Triad Solvated in Explicit Tetrahydrofuran and Its Spectroscopic Signature. *J. Phys. Chem. C* **2018**, *122*, 11288−11299.

(22) Martens, C. C. Nonstationary Time−Series Analysis of Many-Body Dynamics. *Phys. Rev. A: At., Mol., Opt. Phys.* **1992**, *45*, 6914−6917.

(23) Yamauchi, Y.; Nakai, H.; Okada, Y. Short-Time Fourier Transform Analysis of Ab Initio Molecular Dynamics Simulation: Collision Reaction Between $NH_4^+(NH_3)_2$ and NH_3. *J. Chem. Phys.* **2004**, *121*, 11098−11103.

(24) Tamaoki, M.; Yamauchi, Y.; Nakai, H. Short-Time Fourier Transform Analysis of Ab Initio Molecular Dynamics Simulation: Collision Reaction Between CN and C_4H_6. *J. Comput. Chem.* **2005**, *26*, 436−442.

(25) Yamauchi, Y.; Nakai, H. Hybrid Approach for Ab Initio Molecular Dynamics Simulation Combining Energy Density Analysis and Short-Time Fourier Transform: Energy Transfer Spectrogram. *J. Chem. Phys.* **2005**, *123*, 034101.

(26) Otsuka, T.; Nakai, H. Wavelet Transform Analysis of Ab Initio Molecular Dynamics Simulation: Application to Core-Excitation Dynamics of BF_3. *J. Comput. Chem.* **2007**, *28*, 1137−1144.

(27) Yamauchi, Y.; Ozawa, S.; Nakai, H. Ab Initio Molecular Dynamics Simulation of the Energy-Relaxation Process of the Protonated Water Dimer. *J. Phys. Chem. A* **2007**, *111*, 2062−2066.

(28) Akama, T.; Nakai, H. Short-time Fourier Transform Analysis of Real-Time Time-Dependent Hartree-Fock and Time-Dependent Density Functional Theory Calculations with Gaussian Basis Functions. *J. Chem. Phys.* **2010**, *132*, 054104.

(29) Goswami, J. C.; Chan, A. K. *Fundamentals of Wavelets: Theory, Algorithms, and Applications*; Wiley: New York, 1999.

(30) Mallat, S. *A Wavelet Tour of Signal Processing*, 2nd ed.; Elsevier: San Diego, 2009; p 637.

(31) Bahr, J. L.; Kuciauskas, D.; Liddell, P. A.; Moore, A. L.; Moore, T. A.; Gust, D. Driving Force and Electronic Coupling Effects on

Photoinduced Electron Transfer in a Fullerene-Based Molecular Triad. *Photochem. Photobiol.* **2000**, *72*, 598.
(32) Aydin, M. Comparative Study of the Structural and Vibroelectronic Properties of Porphyrin and its Derivatives. *Molecules* **2014**, *19*, 20988−21021.
(33) Agapev, K. B.; Vrubel, I. I.; Polozkov, R. G.; Ivanov, V. K. The Model of the Fullerene C_{60} and its Ions C_{60}^{+}, C_{60}^{-} Pseudopotentials for Molecular Dynamics Purposes. *Eur. Phys. J. D* **2018**, *72*, 1−6.
(34) Mendive-Tapia, D.; Vacher, M.; Bearpark, M. J.; Robb, M. A. Coupled Electron-Nuclear Dynamics: Charge Migration and Charge Transfer Initiated Near a Conical Intersection. *J. Chem. Phys.* **2013**, *139*, 044110.
(35) Huang, K.; Rhys, A.; Mott, N. F. Theory of Light Absorption and Non-Radiative Transitions In F-Centres. *Proceedings of the Royal Society of London. Series A. Mathematical and Physical Sciences* **1950**, *204*, 406−423.
(36) Bittner, E. R.; Lankevich, V.; Gélinas, S.; Rao, A.; Ginger, D. S.; Friend, R. H. How Disorder Controls the Kinetics of Triplet Charge Recombination in Semiconducting Organic Polymer Photovoltaics. *Phys. Chem. Chem. Phys.* **2014**, *16*, 20321−20328.
(37) Bittner, E. R. An Effective Hamiltonian Approach for Donor-Bridge-Acceptor Electronic Transitions: Exploring the Role of Bath Memory. *Condens. Matter Phys.* **2016**, *19*, 1−9.
(38) Lankevich, V.; Bittner, E. R. Relating Free Energy and Open-Circuit Voltage to Disorder in Organic Photovoltaic Systems. *J. Chem. Phys.* **2018**, *149*, 244123.

https://dx.doi.org/10.1021/acs.jpcb.0c00203
J. Phys. Chem. B 2020, 124, 2158−2167